Journal of Materials Chemistry B

Accepted Manuscript

ROYAL SOCIETY OF CHEMISTRY

www.rsc.org/materialsB

Addressing the optimal silver content in bioactive glass systems in terms of BSA adsorption

Klára Magyari[a*], Cristina Gruian[a,b], Béla Varga[c], Raluca Ciceo Lucacel[a], Teodora Radu[a], Heinz-Juergen Steinhoff[b], György Váró[c], Viorica Simon[a], Lucian Baia[a*]

[a]*Babes-BolyaiUniversity, Faculty of Physics &Institute of Interdisciplinary Research in Bio-Nano-Sciences, 400084 Cluj-Napoca, Romania*

[b]*Department of Physics, University of Osnabrueck, 49069 Osnabrueck, Germany*

[c]*Institute of Biophysics, Biological Research Centre of the Hungarian Academy of Sciences, 6071 Szeged, Hungary*

[*]Corresponding author. Tel.: +40-264-405300; Fax: +40-264-591906;
E-mail addresses: lucian.baia@phys.ubbcluj.ro; klara.magyari@ubbcluj.ro

Abstract

Bioactive glasses doped with silver are aimed to minimize the risk of microbial contamination, and therefore, the influence of silver on the bioactive properties is an intense investigated task. However, the information related to the role played by silver, when added to the bioactive glass composition, on the biocompatibility properties is scarce. This aspect is essential as long as the silver content can influence the blood protein adsorption onto glass surface, affecting thus the material biocompatibility. Therefore, from the perspective of the biocompatibility standpoint, the finding of an optimal silver content in a bioactive glass is an extremely important issue. In this study, silver doped bioactive glasses were prepared by melt-derived technique, which eliminates the pores influence in the protein adsorption process. The obtained glasses were characterized by X-ray diffraction, UV-vis, X-ray Photoelectron (XPS) and Fourier Transform Infrared (FT-IR) spectroscopy, and afterwards they were investigated in terms of protein adsorption. Both UV-vis and XPS spectroscopy revealed the presence of Ag^{+} ions in all silver containing samples. By increasing the silver content, metallic Ag^{0} appears, the highest amount being observed for the sample with 1 mol% AgO_2. Electron Paramagnetic Resonance measurements evidenced that the amount of spin labeled serum albumin attached on the surface increases with the silver content. The results obtained by analyzing the information derived from Atomic Force Microscopy and FT-IR measurements indicate that the occurrence of metallic Ag^{0} in the samples structure influences the secondary structure of the adsorbed protein. Based on the results derived from the protein response upon interaction with the investigated glass calcium-phosphate based system it was determined the optimal silver oxide concentration for which the secondary structure of the adsorbed protein is similar with that of the free one. This concentration was found to be 0.5 mol%.

Keywords: silver-bioactive glass; protein adsorption; EPR; FT-IR; AFM

1. Introduction

It is well known that the presence of silver oxide in bioactive glass composition reduces the risk of microbial contamination through leakage of silver ions [1, 2], due to their oligodynamic activity [3, 4]. Phosphate based glasses in the P_2O_5-CaO-Na_2O system have a high level of interest as bone filling material and for scaffold fabrication in bone tissue engineering due to their high solubility and chemical similarity with the inorganic phase of human bone [5]. Ahmed et al [6] demonstrated that incorporation of up to 2 mol% Ag_2O into ternary system P_2O_5-CaO-Na_2O confirms the antibacterial activity. Nevertheless, in the body fluid the release of silver ions is obstructed by the self-assembling of an apatite layer on the bioactive glass surface [7]. Another important aspect that has to be considered for bone tissue engineering type materials is their bioactivity. It was recently shown that phosphate glasses doped with 1 mol% Ag_2O preserve their *in vitro* bioactivity [8].

When biomaterials are introduced into the body they first come into contact with blood proteins, which are spontaneously adsorbed on their surface, and then the cellular attachment, proliferation and migration occurs [9, 10]. Although surface-protein interactions are not completely elucidated, surface chemistry has been shown to play a fundamental role in protein adsorption [11, 12]. Several studies have shown that the conformation of proteins changes upon adsorption onto the material surface, affecting thus the material biocompatibility and further the cellular interaction [9-11, 13-15]. It is already known that bovine serum albumin (BSA) displays high binding affinity towards silver nanoparticles, which in turn trigger changes in its spatial structure [16-18]. The changes in secondary structure of BSA may be thus affected by the silver content in the glasses.

The role played by silver in the antibacterial [6, 19-22] and bioactive [8, 23, 24] behaviour of the glasses was intensely studied lately, but little work has been focused on evaluating the biocompatibility of these glasses. Consequently, this study aims to investigate the way silver content in bioactive glass influences protein adsorption, as first event occurring upon interaction with body fluids. Furthermore, it is proposed to determine the optimal Ag_2O concentration in the bioactive glass, in terms of interaction with proteins. To this end, bovine serum albumin (BSA) was considered as model protein, since it displays high structural homology with human serum albumin [12]. Serum albumin is the most abundant protein, accounting for 60-70% for the measured plasma proteins and is the first protein surrounding foreign bodies when they come in contact with the blood [25]. The albumin structure is predominantly helical (Fig. 1) with the remaining polypeptides occurring in turns or flexible regions between the subdomains [26]. Albumin is considered to greatly reduce the acute inflammatory response to biomaterials[27].

It has already been demonstrated that the sol-gel derived bioactive glass 45S5 eluted more protein per unit mass than the melt-derived 45S5 glass [28]. To eliminate the influence of porosity on the adsorption process, in the present study bioactive glasses were prepared by the conventional melt quenching method. Prior to protein attachment, samples of $P_2O_5 \cdot CaO \cdot Na_2O$ system doped with Ag_2O were subjected to structural analysis by X-ray diffraction (XRD), UV-Vis, X-Ray Photoelectron Spectroscopy (XPS) and Fourier Transform Infrared (FT-IR) spectroscopy. Conformational changes

induced in the BSA structure as consequence of interaction with the investigated samples were followed by FT-IR spectroscopy and Atomic Force Microscopy (AFM). Spin labeling in combination with Electron Paramagnetic Resonance (EPR) spectroscopy was employed to quantify the amount of protein attached on each glass sample. EPR spectroscopy provides detailed structural, dynamic and quantitative information for biomolecules not only in solution but can also be applied to adsorbed or encapsulated spin labeled proteins as reported recently [29-31]. This method enables to determining the protein amount in the overall mass of the sample, by counting the number of spins contributing to the paramagnetic signal. The EPR spectra were further used to monitor local structural changes in BSA following the adsorption process. In the present study (4-(2-Iodoacetamido)-2,2,6,6-tetramethyl-1-piperidinyloxy) iodoacetamide (IA) spin label was used to label the cysteine residue located in position 34 of bovine serum albumin, which contains the unique free thiol group that is not involved in a disulfide bridge (Fig. 1). BSA adsorption onto the investigated systems was explored in conditions close to its physiological environment phosphate buffer solution at pH 7.4), by following the EPR signal of the paramagnetic centre attached.

Fig. 1

- **Materials and Methods**

1.1. Formation of glass

The $60P_2O_5 \cdot 20CaO \cdot (20-x) \cdot Na_2O \cdot xAg_2O$ with x=0, 0.3, 0.5, 0.8 and 1 mol% bioactive glasses were prepared by conventional melt quenching method using $NH_4 \cdot H_2PO_4$, $CaCO_3$, $Na_2CO_3 \cdot 10H_2O$and $AgNO_3$ as starting materials. The mixtures corresponding to the desired compositions were melted in air, in sintered corundum crucibles, in an electric furnace at 1200°C for 30 min. The melts were quickly cooled at room temperature by pouring and pressing between two copper plates.

Contact angle was measured using a drop shape analysis in the sessile drop method with 2 µl water for the characterization of the surfaces.

1.2. Protein adsorption

Bovine serum albumin (BSA) (Sigma–Aldrich, molar mass 69 kDa) solutions of different concentrations were prepared in phosphate buffer solution (PBS) pH 7.4 to test the protein adsorption by means of different investigation methods. Before protein adsorptions the samples were cleaned with plasma cleaner.

Glass powders for FT-IR and glass pieces for AFM measurements were immersed in BSA solutions of 100 µM (~6.9 mg/ml) and 7 µM (~ 0.5 mg/ml) respectively and afterwards placed in an incubator at constant temperature of 37°C for 30 min. The solution was then removed from the samples, rinsed three times with PBS, and air dried.

For spin labeling procedure a solution of 100 μM bovine serum albumin in phosphate buffer (pH 7.4) was incubated for 48 hours at 37°C with 6-fold molar excess of (4-(2-Iodoacetamido)-2,2,6,6-tetramethyl-1-piperidinyloxy) spin label. Unbound IA was removed by repeated dilution steps with sodium phosphate buffer, pH 7.4, using centrifugal filter units with 30 kDa molecular weight cut-off (Amicon/ Millipore, Carringtwohill, Co. Cork, Ireland). Labeling efficiency (spin label per protein molecule) was determined to be 100% (±5%). Considering the location of cys34 residue, which is hidden in a hydrophobic crevice and, therefore, not so easy accessible, we assume that this high value of spin label efficiency is given by the additional labeling of other thiol groups. BSA has 35 cysteines in total, 34 of them being involved in disulphide bridges. It was previously shown that between pH 7 and pH 10 a gradual reduction of S-S bonds occurs in bovine serum albumin, so that up to three disulfide bonds are reducible in the protein, becoming thus available for spin labeling [32, 33]

For protein adsorption experiments, the glass pieces were milled to micrometric size particles. The powder samples (150 mg) were afterwards incubated for 30 min at 37°C in spin labeled BSA solution (100 μM). Afterwards, the samples were washed three times with buffer solution, to remove the unattached protein molecules.

1.3. Methods

X-ray Diffraction The X-ray diffraction analysis was carried out on a Shimadzu XRD-6000 diffractometer using CuKα radiation (λ=1.54), with Ni-filter.

UV-vis Spectroscopy absorption measurements were performed with Analytic Jena Specord 250 plus UV-Vis spectrometer. The spectral resolution was of 2 nm.

X-Ray Photoelectron Spectroscopy XPS spectra were recorded with a SPECS PHOIBOS 150 MCD system employing a monochromatic Al-K_α source (1486.6 eV), a hemispherical analyser and charge neutralization device. Samples were fixed on a double-sided carbon tape and care was taken to ensure that the sample particles covered the tape. Experiments were performed by operating the X-ray source with a power of 250 W, while the pressure in the analyse chamber was in the range of 10^{-9}- 10^{-10} mbar. The binding energy scale was charge referenced to the C 1s at 284.6 eV. Elemental composition was determined from survey spectra acquired at pass energy of 100 eV. High resolution spectra were obtained using analyzer pass energy of 30 eV. Analysis of the data was carried out with Casa XPS software. A Shirley background was used for all curve-fitting along with the Gaussian/Lorentzian product form (70% Gaussian and 30% Lorentzian).

FT-IR Spectroscopy The FT-IR spectra of the glass samples were recorded in reflection configuration in the range 4000-400 cm^{-1} with spectral resolution of 4 cm^{-1} using a Jasco FT-IR-6000 spectrometer and KBr pellet technique. The FT-IR spectra of glasses after protein adsorption were recorded using a Jasco IRT-5000 FT-IR microscope coupled to a Jasco FT-IR-6000 spectrometer in reflection configuration in the range 4000-650 cm^{-1} with a resolution 4 cm^{-1}, using the x32 Cassegranian objective imaged a sample

area of ~50 × 50 μm^2. The recorded spectra were smoothed by a 9-point Savitzky-Golay smoothing function for background correction. Second-derivative spectral analysis was performed by using the JASCO Spectra Manager in order to locate the position of the overlapped components of amide I, which were further assigned to different secondary structures. The bands were deconvoluted with a Gaussian band profile, a linear baseline between 1600 cm^{-1} and 1710 cm^{-1} being previously applied. The secondary structure composition was determined from the areas of the individually assigned components and their fraction of the total area.

EPR Spectroscopy X band cw-EPR experiments were performed using a commercially available Mini Scope benchtop EPR spectrometer (MS200; Magnettech GmbH, Berlin, Germany) with a rectangular TE102 resonator. Due to heat production in the resonator during operation, the sample environment was fluxed with gaseous nitrogen keeping the temperature stable. The spectrometer settings were as follows: the microwave power was set to 10 mW; the B-field modulation amplitude was 0.15 mT. EPR glass capillaries of 1 mm inner diameter (i.d.) were filled with sample volumes of 20 µl, considering that the EPR active volume of the sample tube is 15 µl. The integrated EPR absorption signal is directly proportional to the spin concentration in the sample and was used to calculate the amount of the protein attached on the investigated systems. As reference spin probe, 2,2,6,6-Tetramethyl-1-piperidinyloxy (TEMPO) of 100 µM concentration was used.

Atomic Force Microscopy AFM measurements were carried out on an Asylum MFP-3D head and controller (Asylum Research, Santa Barbara, CA). The driver program MFP-3D Xop was written in IGOR Pro software (version 5.04b, Wavemetrics, Lake Oswego, OR). The measurements were carried out with AC240 rectangular silicon cantilevers, with tetrahedral tips (Olympus, Optical Co. Ltd. Tokyo, Japan). The spring constant for each cantilever was determined by thermal calibration [34]. The measurements were carried out in AC (noncontact) mode in air at room temperature. Typically, 512x512 point scans were taken at a scan rate 1 Hz per line. Both trace and retrace images were recorded and compared.

2. Results and Discussion

2.1. Structural characterization

The obtained samples with $60P_2O_5$ 20CaO (20-x)Na_2O xAg_2O (x=0, 0.3, 0.5, 0.8 and 1 mol%) composition prepared by conventional melt quenching method were transparent and colourless. The X-ray diffraction patterns consist of a very broad peak (Fig. 2) and confirm the vitreous character of all samples.

Fig. 2

In order to obtain further insight into the structure of the investigated glass samples, UV-vis absorption spectra were recorded. The silver atoms, ions, and clusters exhibit different optical properties that can be

evidenced by means of UV–vis spectroscopy. Thus, the electronic transitions involving the Ag^+ ion are visible in the 190-230 nm spectral range, the electronic transitions of metallic Ag^0 appear in the 250-330 nm spectral range, while isolated and aggregated Ag nanoparticles absorb at wavelength higher than 400 nm [23, 35, 36]. The UV-vis absorption spectra recorded on the investigated samples evidenced absorption bands only for the silver containing glasses (Fig. 3). The glasses with lower concentration of silver (x=0.3 and 0.5), exhibit only absorption bands in the 190-230 nm spectral range, associated with the presence of Ag^+ ion, although the sample containing 0.5 %mol AgO_2 slightly exhibits the presence of metallic Ag^0. However, as the silver amount increases (x=0.8 and 1) close to the absorption band recorded for the Ag^+ ion, the UV-vis spectra reveal the presence of the metallic Ag^0, as shown by the presence of the electronic absorption signal that occurs in the 250-300 nm spectral range.

Fig. 3

To investigate the chemical state of silver in these glasses a XPS analysis was performed. The Ag 3d spectrum consists of a doublet for the Ag $d_{5/2}$ and Ag $d_{3/2}$ components due to spin-orbit splitting, at the binding energy 368.6 and 374.6 eV, respectively (Fig. 4) [23, 37, 38]. To further examine the chemical state of silver in the investigated glass with 0.5, 0.8 and 1 mol% Ag_2O, the Ag 3d photoelectron peaks were deconvoluted. Silver content of the glass with 0.3% Ag_2O is very small, thus the deconvolution could not be performed.For the Ag $d_{5/2}$ component two contributions were considered centred at binding energies of 368.6 and 367.2 eV and are assigned to Ag^0 and Ag^+, respectively [37]. By calculating the peak area ratios of the deconvoluted peaks in the sample with x=0.8 it was determined that about 66.71% of the silver atoms are in the Ag^0 chemical state, while 32.7% are in the Ag^+ chemical state. Higher percentage of Ag^0 metallic (87.1%) is in turn present in the sample with x=1. The deconvolution of Ag 3d photoelectron peaks for the sample containing 0.5 mol% silver oxide provides only one component, attributed to the Ag^+ chemical state. These findings confirm the results obtained by Uv-vis spectroscopy, i.e. with increasing the silver content in the glass the amount of metallic silver increases.

Fig. 4

The FT-IR spectra of the obtained glass samples have characteristic absorption bands of phosphate based glasses (Fig. 5) [6, 8, 36, 39-41]. The bands in the region 400-600 cm^{-1} can be attributed to bending vibrations of bridging phosphorus such as O-P-O and/or O=P-O [6, 39, 40]. The IR bands and shoulders observed at around 772 and 715 cm^{-1} for x=0 are attributed to the P-O-P bending and asymmetric vibrations, respectively [40, 41].

The absorption band at around 905 cm^{-1} is attributed to the $(PO_4)^{3-}$ symmetric stretching vibrations, indicating that a considerable part of the phosphate network still remains linked even after addition of a relatively high amount of silver [36]. The band observed at around 1280 cm^{-1} can be assigned

to the P=O stretching vibrations [40], while the bands at approximately 1100 cm^{-1} and at 1020 cm^{-1} are due to $(PO_3)^{2-}$ stretching vibrations [36, 40].

Fig. 5

2.2. Protein adsorption

Wettability of the surface plays an important role in the in the conformational changes in which a protein undergoes during adsorption on a surface. In order to clarify this aspect, the contact angle of the studied surfaces was measured. Since in all the cases the value determined for the contact angle was 37°±3, one can infer that the used Ag_2O content does not affect the hydrophobic character of the surface.

After BSA adsorption the FT-IR spectra of the samples containing Ag_2O show the presence of the two characteristic bands of proteins: amide I band at 1650 cm^{-1} and amide II band at 1550 cm^{-1} (Fig. 6). The integrated area of amide I of BSA adsorbed onto the glass surfaces was normalized to the absorption band at 1280 cm^{-1} and subjected to quantitative comparison (Fig. 7) by assuming that there is a small probability that this type of vibration to be affected by the silver addition. The maximum value of the integrated area has been obtained for the sample with 0.5 mol% silver oxide content.

It was reported that the change of the intensities ratio of amide I/II bands indicates that the secondary structure of the protein might be affected [11, 42]. In the case of the investigated samples the amide I/II intensity ratio increases progressively (from 2.1 for 0.5 mol %Ag_2O to 2.7 for 1 mol%Ag_2O) suggesting that the secondary structure of the protein is gradually, more intense affected, as the silver content increases. The most important question that arises now is related to the role played by the silver content on the induced conformational changes. In order to get more insights into the mentioned aspect EPR measurements were further performed.

Fig. 6

Fig. 7

The EPR spectrum of spin labeled BSA reveals the presence of two spectral components clearly visible in the lower field spectral line (Fig. 8). As discussed in the Materials and methods section, besides the free thiol from position 34, additional cysteines were labeled, as one to three disulphide bonds were broken in each protein, as consequence of the pH value used. Component *I* (immobile) represents a fraction of the nitroxide population having the spin label reorientational freedom restricted due secondary and tertiary interactions, as result of the Cys34 location in a hydrophobic crevice of 9.5–10 Å depth [43] and/or the local restrictions of the other labelled disulphide bridges (it was previously shown that all 17 disulphide bonds in BSA have buried locations within the protein molecule [26]). The resulting EPR

spectrum is characterized by broad lines and large apparent hyperfine splittings. Contrarily, component *M* (mobile) is characterized by narrow linewidth of the central line and small apparent hyperfine splitting, representing a nitroxide subpopulation with higher spin label mobilities, indicating that the nitroxide moiety is more free in the solvent.

Upon adsorption on the samples surface, the immobile component increases on the account of the mobile component (see inset of Fig. 8), evidencing local conformational changes in the vicinity of the labeledcysteines, as consequence of the adsorption process. The linewidth increase observed in the lower field spectral line for all the EPR spectra recorded in adsorbed state (shown by arrow in Fig. 8) suggests that the movement of the entire BSA molecule is hampered by the interaction with the samples substrate. As silver concentration increases, the EPR spectra show stronger immobilization of spin labels on the substrate, indicating enhanced interaction of the BSA molecule on the samples with higher silver content. This behaviour was previously reported on methemoglobin attached on silver containing bioactive glass, and it was attributed to the interaction between silver ions and thiol groups in proteins [23, 24]. Other study also emphasized the strong interaction between silver nanoparticles and sulphur-containing peptides/amino acids[44]. Since the free thiol groups in the BSA molecule were blocked by the spin label, we assume that additional thiol groups involved in disulfide bridges in the BSA molecule are broken during the adsorption process. The aggressiveness of this process is strongly dependent on the silver content in the sample: over 0.5 mol% Ag_2O, the protein suffers more severe conformational changes. It might be possible that on samples with higher silver content (0.8 and 1 mol% Ag_2O) the surroundings of the labelled cysteines are completely unfolded, and thus these regions have direct contact with the bioactive glass surface. This would imply that at silver oxide contents higher than 0.5 mol%, the interaction between bioactive glass and BSA results in unfolding of a large fraction of the protein structure. Furthermore, the amount of the protein attached on the sample can be also interpreted as a result of the strong interaction owed to the presence of silver in the sample. As silver content increases, more protein attaches on the sample surface (see Fig. 9). No protein was found to be attached on the sample without silver content, most probably because the marker concentration from the adsorbed protein was under the detection limit. This is clear evidence on the fact that the main interaction between the BSA molecule and the samples surface occurs especially through the medium of silver ions. On the other hand, the missing of a signal from the protein attached on the silver free glass suggest that the best way of interpreting the achieved data is from qualitative perspective.

Fig. 8

Fig. 9

The secondary structure conformation of the BSA after adsorption on the glass surfaces was analysed by deconvolution of the amide I absorption band from the FT-IR spectrum [42]. The secondary structure of lyophilized BSA is typical, dominated by α helices (1649-1657 cm^{-1}), but it also contains a small amount of

β-sheets (1618-1641 and 1674-1695 cm^{-1}) and β-turn (1662-1686 cm^{-1}) structure [45]. After adsorption, in all cases, a new band appears around 1608 cm^{-1}that can be associated with the existence of β-sheet aggregation/amino acid side chain residues [46]. The secondary structure of BSA, after its adsorption on the glass with 0.5 mol% Ag_2O, evidenced only minor changes that are within the errors limit. In contrast, in the case of samples with 0.8 and 1 mol% Ag_2O, one can observe that BSA loses a large fraction of its helical structure and a concurrent increase in β-sheet and β-turn structure components occurs (Fig. 10, 11). These results support the hypothesis highlighted by EPR spectroscopy, that a large fraction of the protein structure is unfolded on the bioactive glasses with silver contents higher than 0.5 mol%. Interestingly, the UV-vis spectra showed that metallic Ag^0 appears on these samples (Fig. 3). Concerning the sample without silver oxide content one observes that the secondary structure of BSA is affected as a consequence of a small amount of protein adsorption.

Fig. 10

Fig. 11

To visualize the BSA adsorption on the glass surfaces, the AFM technique was used (Fig. 12). In order to compare the surface changes induced by BSA adsorption the surface roughness was determined from 1x1 μm^2 images (Fig. 13) [47, 48]. The AFM images revealed that the surface roughness begins to increase with the addition of silver oxide in the glasses, peaking at 0.5mol%, after which it begins to decrease (Fig. 13). These results support the hypothesis highlighted by FT-IR and EPR spectroscopy, namely that the BSA structure unfolds on the high (x=0.8 and x=1) silver content samples. The attached protein layer is, therefore, more uniform on these two samples, resulting in increase of surface smoothness.

All results presented in this study suggest that increasing the silver content in glass samples increases the albumin adsorption on the surface, but metallic Ag^0 appearance in the glass samples affects the protein secondary structure. This is in agreement with results obtained by the other researcher groups that silver ions are active species in the biological system, since BSA can bind free silver ions, thus reducing its cell toxicity [17]. The negatively charged surface such as OH, SH and COOH that activate the coagulation cascade, via the adsorption on various sites like those represented by the silver species, could also represents a possible reason for the important conformational change of the protein that appears for high silver content. Nevertheless, for the deep understanding of the role played by the silver amount present in the composition of a bioactive glass on the protein conformational changes other in detail investigations are needed.

Fig. 12

Fig. 13

3. Conclusions

The $60P_2O_5 \cdot 20CaO \cdot (20-x) \cdot Na_2O \cdot xAg_2O$ ($0 \leq x \leq 1$mol %) melt-derived bioactive glass system was studied with respect to the influence of silver content on serum albumin adsorption. The XPS and UV-vis spectra revealed that in the samples with the lowest Ag_2O content (x= 0.3 and 0.5) only Ag^+ ions are present, while metallic Ag^0 starts to appear for Ag_2O content exceeding 0.8mol%. Room temperature EPR spectra of spin labelled protein revealed that silver content in the sample increases the adsorption potential of albumin on the sample surface. Nevertheless, the appearance of metallic Ag^0 on samples with 0.8 and 1 mol% Ag_2O results in severe alteration of the BSA secondary structure, as a consequence of protein unfolding, and this effect was revealed by EPR, FT-IR spectroscopy and AFM. All results presented here suggest that the optimal silver oxide concentration in the investigated bioactive glass system for which the secondary structure of the adsorbed protein is similar with that of the free one is 0.5 mol%. This silver content represents the best compromise for the two important issues related to the protein adsorption process on the involved bioactive glass surface: the amount of the attached protein and the lack of conformational changes induced in the protein structure.

Acknowledgments

CG and HJS gratefully acknowledge the support by the DAAD programme “Ostpartnerschaften”.

References

1. J. J. Blaker, A. R. Boccaccini and S. N. Nazhat, *Journal of biomaterials applications*, 2005, 20, 81-98.
2. M. Bellantone, H. D. Williams and L. L. Hench, *Antimicrobial Agents and Chemotherapy*, 2002, 46, 1940-1945.
3. S. S. Djokie and R. E. Burrell, *Journal of the Electrochemical Society*, 1998, 145, 1426-1431.
4. S. Di Nunzio, C. Vitale Brovarone, S. Spriano, D. Milanese, E. Verné, V. Bergo, G. Maina and P. Spinelli, *Journal of the European Ceramic Society*, 2004, 24, 2935-2942.
5. A. Hoppe, N. S. Guldal and A. R. Boccaccini, *Biomaterials*, 2011, 32, 2757-2774.
6. A. A. Ahmed, A. A. Ali, D. A. R. Mahmoud and A. M. El-Fiqi, *Solid State Sciences*, 2011, 13, 981-992.
7. V. Simon, C. Albon and S. Simon, *Journal of Non-Crystalline Solids*, 2008, 354, 1751-1755.
8. R. Ciceo Lucacel, A. O. Hulpus, V. Simon and I. Ardelean, *Journal of Non-Crystalline Solids*, 2009, 355, 425-429.
9. R. A. Latour Jr, *Taylor & Francis, New York*, 2005, DOI: 10.1081/e-ebbe-120041856, 1-15.
10. K. Wang, C. Zhou, Y. Hong and X. Zhang, *Interface focus*, 2012, 2, 259-277.
11. P. Roach, D. Farrar and C. C. Perry, *Journal of the American Chemical Society*, 2005, 127, 8168-8173.
12. X. M. He and D. C. Carter, *Nature*, 1992, 358, 209-2015.
13. E. Vanea, K. Magyari and V. Simon, *Journal of Optoelectronics and Advanced Materials*, 2010, 12, 1206-1212.
14. K. Magyari, O. Popescu and V. Simon, *Journal of Materials Science: Materials in Medicine*, 2010, 21, 1913-1920.

15. K. Magyari, L. Baia, O. Popescu, S. Simon and V. Simon, *Vibrational Spectroscopy*, 2012, 62, 172-179.
16. N. Shahabadi, M. Maghsudi and Z. Ahmadipour, *Spectrochimica Acta Part A: Molecular and Biomolecular Spectroscopy*, 2012, 92, 184-188.
17. S. Kittler, C. Greulich, J. S. Gebauer, J. Diendorf, L. Treuel, L. Ruiz, J. M. Gonzalez-Calbet, M. Vallet-Regi, R. Zellner, M. Koller and M. Epple, *Journal of Materials Chemistry*, 2010, 20, 512-518.
18. R. Liu, F. Sun, L. Zhang, W. Zong, X. Zhao, L. Wang, R. Wu and X. Hao, *Science of the Total Environment*, 2009, 407, 4181-4188.
19. A. Vulpoi, V. Simon, H. Ylänen and S. Simon, *Journal of Composite Materials*, 2014, 48, 63-70.
20. A. Balamurugan, G. Balossier, D. Laurent-Maquin, S. Pina, A. H. Rebelo, J. Faure and J. M. Ferreira, *Dental materials : official publication of the Academy of Dental Materials*, 2008, 24, 1343-1351.
21. S. P. Valappil, M. Coombes, L. Wright, G. J. Owens, R. J. M. Lynch, C. K. Hope and S. M. Higham, *Acta biomaterialia*, 2012, 8, 1957-1965.
22. R. K. Kunkalekar, M. S. Prabhu, M. M. Naik and A. V. Salker, *Colloids and surfaces. B, Biointerfaces*, 2013, 113C, 429-434.
23. A. Vulpoi, C. Gruian, E. Vanea, L. Baia, S. Simon, H. J. Steinhoff, G. Goller and V. Simon, *Journal of biomedical materials research. Part A*, 2012, 100, 1179-1186.
24. C. Gruian, A. Vulpoi, E. Vanea, B. Oprea, H. J. Steinhoff and S. Simon, *The journal of physical chemistry. B*, 2013, 117, 16558-16564.
25. A. Krajewski, R. Malavolti and A. Piancastelli, *Biomaterials*, 1996, 17, 53-60.
26. D. C. Carter and J. X. Ho, *Academic Press INC, San Diego*, 1994.
27. L. Tang and J. W. Eaton, *American Journal of Clinical Patology*, 1995, 103, 466-471.
28. M. S. Bahniuk, H. Pirayesh, H. D. Singh, J. A. Nychka and L. D. Unsworth, *Biointerphases*, 2012, 7, 41.
29. K. Jacobsen, W. L. Hubbell, O. P. Ernst and T. Risse, *Angewandte Chemie* 2006, 45, 3874-3877.
30. C. Gruian, A. Vulpoi, H. J. Steinhoff and S. Simon, *Journal of Molecular Structure*, 2012, 1015, 20-26.
31. E. Vanea, C. Gruian, C. Rickert, H. J. Steinhoff and V. Simon, *Biomacromolecules*, 2013, 14, 2582-2592.
32. T. Peters Jr, *Academic press*, 1995.
33. M. T. Stankovich and A. J. Bard, *Journal of Electroanalytical Chemistry and Interfacial Electrochemistry*, 1978, 86, 189-199.
34. J. L. Hutter and J. Bechhoefer, *Review of Scientific Instruments*, 1993, 64, 1868.
35. J. Lu, J. Bravosuarez, A. Takahashi, M. Haruta and S. Oyama, *Journal of Catalysis*, 2005, 232, 85-95.
36. L. Baia, D. Muresan, M. Baia, J. Popp and S. Simon, *Vibrational Spectroscopy*, 2007, 43, 313-318.
37. O. Akhavan, M. Abdolahad, Y. Abdi and S. Mohajerzadeh, *Journal of Materials Chemistry*, 2011, 21, 387-393.
38. T. Radu, D. Benea, R. Ciceo-Lucacel, L. Barbu-Tudoran and S. Simon, *The Journal of Physical Chemistry C*, 2012, DOI: 10.1021/jp306035n, 17975−17979.
39. R. Ciceo Lucacel, O. Ponta and V. Simon, *Journal of Non-Crystalline Solids*, 2012, 358, 2803-2809.
40. Y. M. Moustafa and K. El-Egili, *Journal of Non-Crystalline Solids*, 1998, 240, 144-153.
41. K. El-Egili, H. Doweidar, Y. M. Moustafa and I. Abbas, *Physica B: Condensed Matter*, 2003, 339, 237-245.
42. A. Barth, *Biochimica et biophysica acta*, 2007, 1767, 1073-1101.

43. M. Oblak, A. Prezelj, S. Pecar and T. Solmajer, *Zeitschrift fur Naturforschung. Section C, Journal of biosciences.*, 2004, 59, 880-886.
44. A. V. Novikov, R. A. Bublyaev, N. V. Krasnov, Y. P. Kozmin and O. A. Mirgorodskaya, *Protein and Peptide Letters*, 2010, 17, 1392-1397.
45. S. Nafisi, G. Bagheri Sadeghi and A. PanahYab, *Journal of photochemistry and photobiology. B, Biology*, 2011, 105, 198-202.
46. S. Y. Lin, Y. S. Wei, T. F. Hsieh and M. J. Li, *Biopolymers*, 2004, 75, 393-402.
47. N. Seidel, J. Sitterberg, W. Vornholt, U. Bakowsky, M. Keusgen and T. Kissel, *Biomaterials*, 2012, 33, 1929-1938.
48. M. Holmberg and X. Hou, *Colloids and surfaces. B, Biointerfaces*, 2011, 84, 71-75.

Figure caption

Fig. 1 The crystal structure of bovine serum albumin dimer obtained by X-ray crystallography (pdb 4F5S). The two monomers are coloured in cyan and blue, respectively. Each native cysteine from position 34 is coloured in red and the atoms are shown as ball and stick. The region surrounding the two cys34 positions is enlarged in the lower part.

Fig. 2 XRD patterns of the $60P_2O_5{\cdot}20CaO{\cdot}(20\text{-}x){\cdot}Na_2O{\cdot}xAg_2O$ glass samples

Fig. 3 UV-VIS spectra of the $60P_2O_5{\cdot}20CaO{\cdot}(20\text{-}x){\cdot}Na_2O{\cdot}xAg_2O$ glass samples

Fig. 4 Deconvolution of Ag 3d XPS spectra of the $60P_2O_5{\cdot}20CaO{\cdot}(20\text{-}x){\cdot}Na_2O{\cdot}xAg_2O$ glass samples

Fig. 5 FT-IR spectra of the $60P_2O_5{\cdot}20CaO{\cdot}(20\text{-}x){\cdot}Na_2O{\cdot}xAg_2O$ glass samples

Fig. 6 FT-IR spectra of the $60P_2O_5{\cdot}20CaO{\cdot}(20\text{-}x){\cdot}Na_2O{\cdot}xAg_2O$ glass samples after BSA adsorption

Fig. 7 FT-IR spectra (a) and integrated area (b) of the amide I absorption band of BSA recorded after adsorption onto $60P_2O_5{\cdot}20CaO{\cdot}(20\text{-}x){\cdot}Na_2O{\cdot}xAg_2O$ glass surfaces and normalized to the absorption band at 1280 cm^{-1}. The normalized amide I absorption bands are displayed in descending order, as shown by the arrow.

Fig. 8 Room temperature cw-EPR spectra of spin labeled BSA after adsorption on the investigated samples, normalized to amplitude. Upper right inset: the low field spectral line of the normalized cw-EPR spectra recorded for spin labeled BSA before (black) and after adsorption onto the investigated samples. The grey line was recorded for BSA adsorbed the sample containing 0% Ag. The black arrow shows the linewidth increase of the low filed line, after adsorption. The mobile and immobile components visible in the lower field spectral lines are depicted with *M* and *I*, respectively (inset).

Fig. 9 BSA attached in the EPR active volume (µg) after adsorption onto the investigated samples. Errors are estimated to ± 2%, due to experimental settings and uncertainties in baseline substraction.

Fig. 10 Deconvolution of the amide I (1700-1600 cm^{-1}) absorption band of the lyophilized BSA, before and after its adsorption on the bioactive $60P_2O_5{\cdot}20CaO{\cdot}(20\text{-}x){\cdot}Na_2O{\cdot}xAg_2O$ glass samples surface

Fig. 11 Distribution of secondary structures in lyophilized and adsorbed BSA onto $60P_2O_5{\cdot}20CaO{\cdot}(20\text{-}x){\cdot}Na_2O{\cdot}xAg_2O$ glass samples surface

Fig. 12 AFM images of the $60P_2O_5{\cdot}20CaO{\cdot}(20\text{-}x){\cdot}Na_2O{\cdot}xAg_2O$ glass samples; height images before adsorption (a); height images after BSA adsorption (b); amplitude images before adsorption (c) and amplitude images after BSA adsorption (d)

Fig. 13 Root-mean-square (RMS) roughness before and after BSA adsorption determined by AFM from 1x1µm^2 images

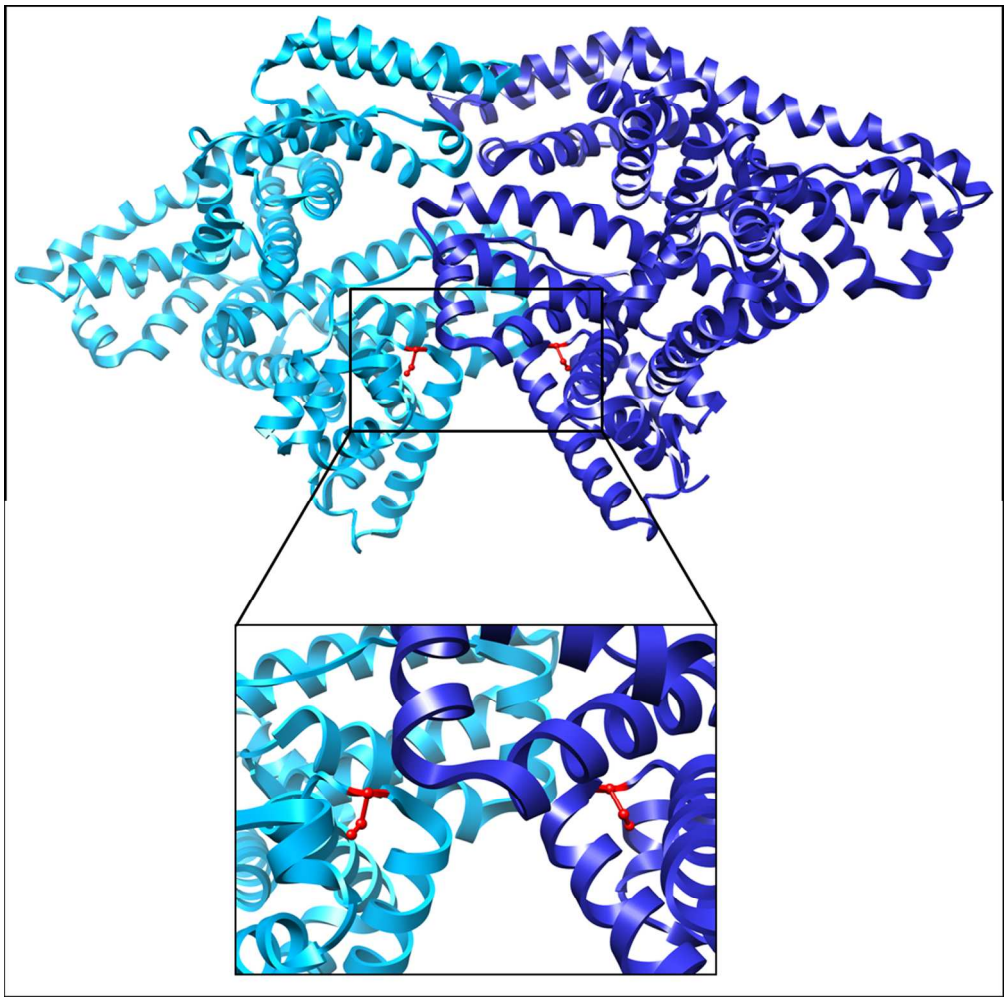

Figure 1
184x182mm (300 x 300 DPI)

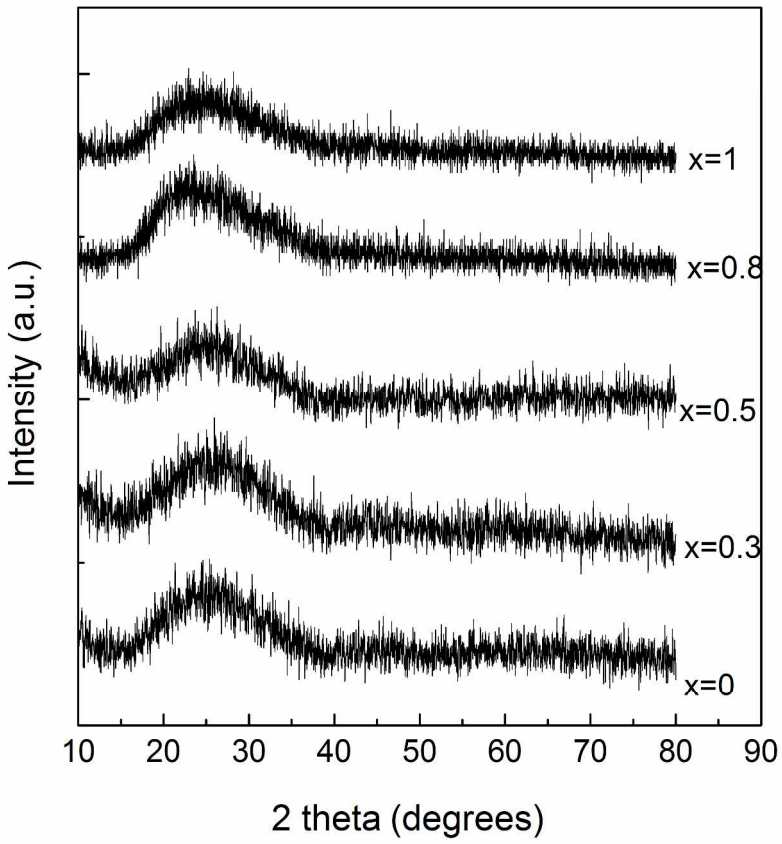

Figure 2
271x271mm (300 x 300 DPI)

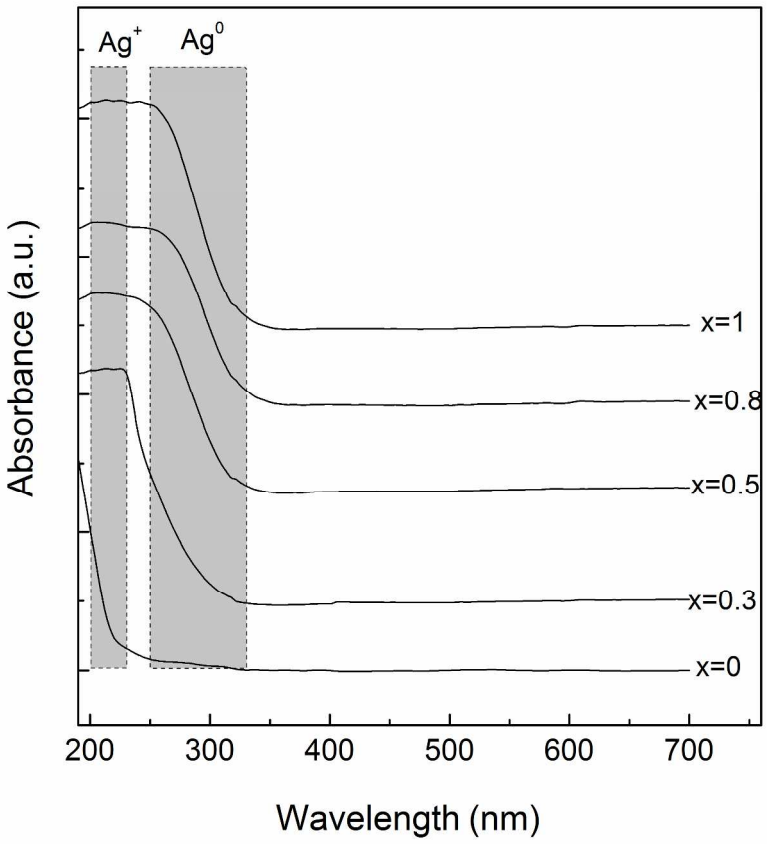

Figure 3
279x279mm (300 x 300 DPI)

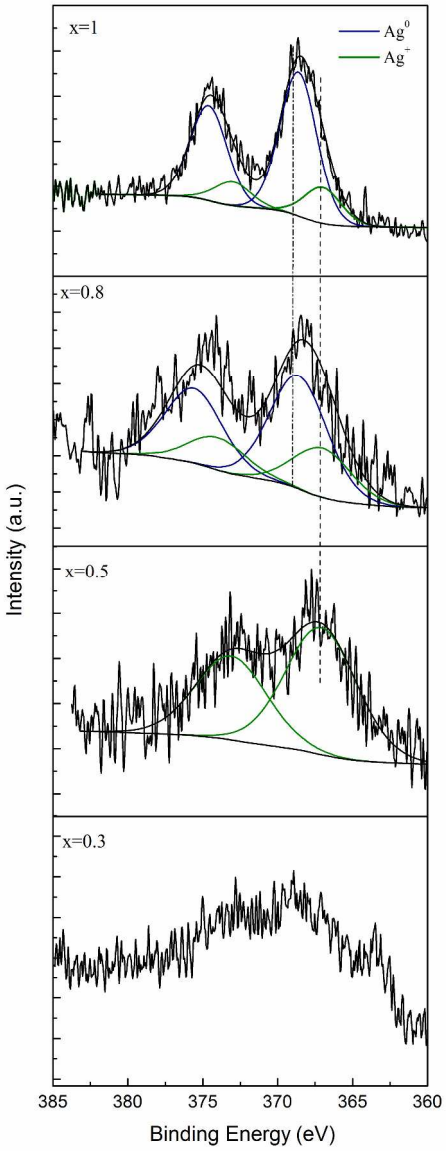

Figure 4
199x480mm (300 x 300 DPI)

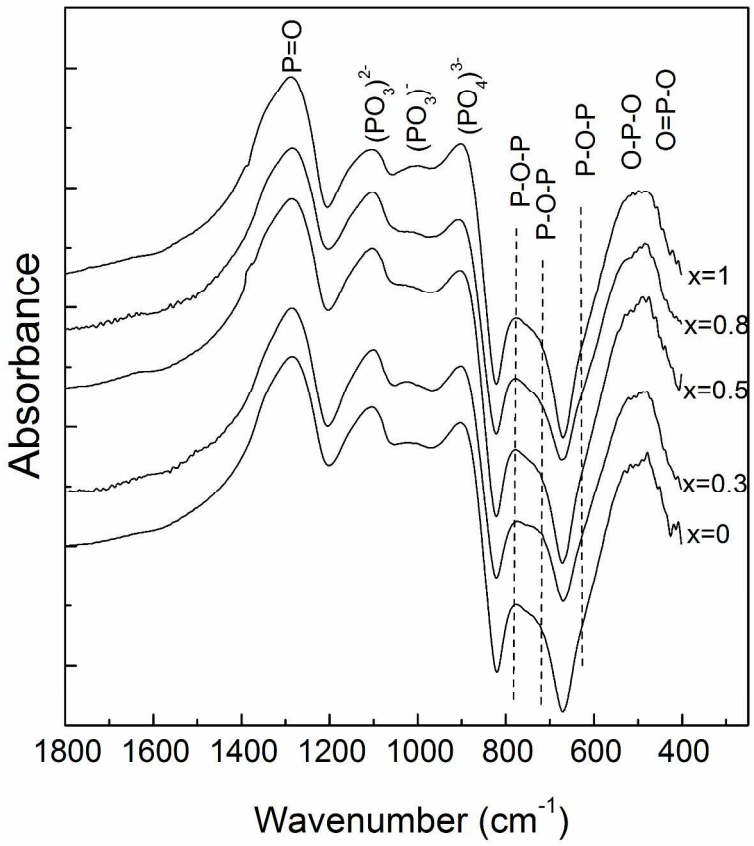

Figure 5
271x271mm (300 x 300 DPI)

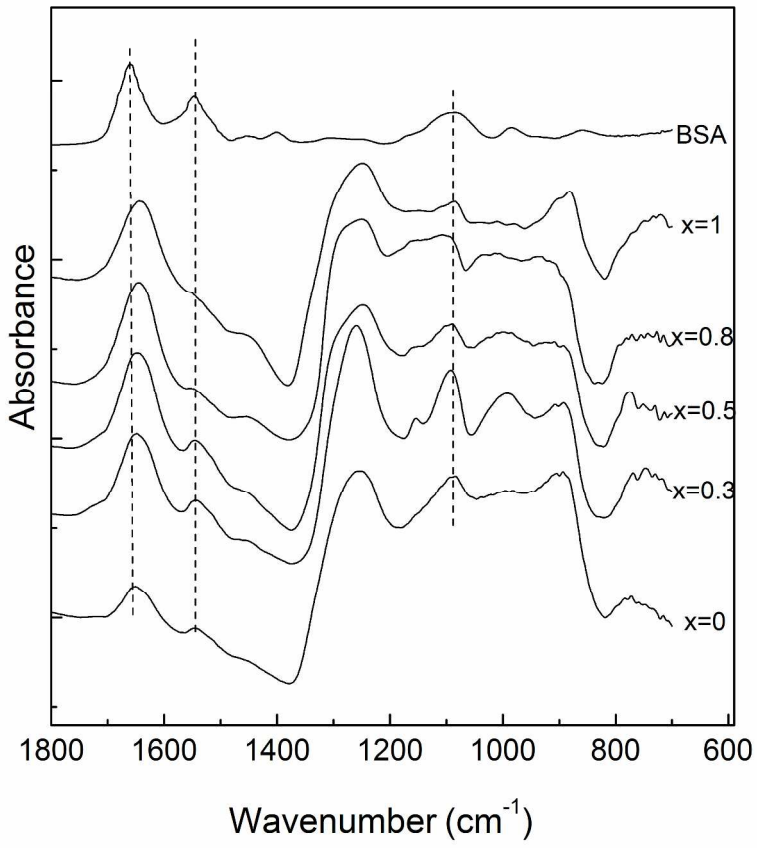

Fig. 6
279x279mm (300 x 300 DPI)

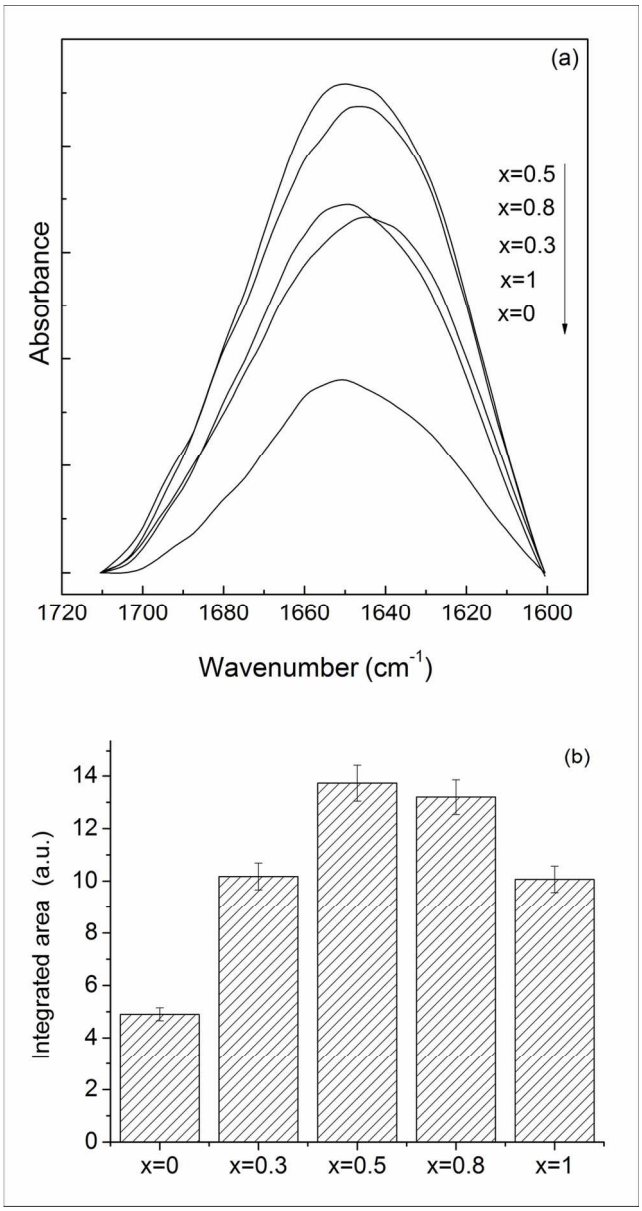

Fig. 7
160x302mm (300 x 300 DPI)

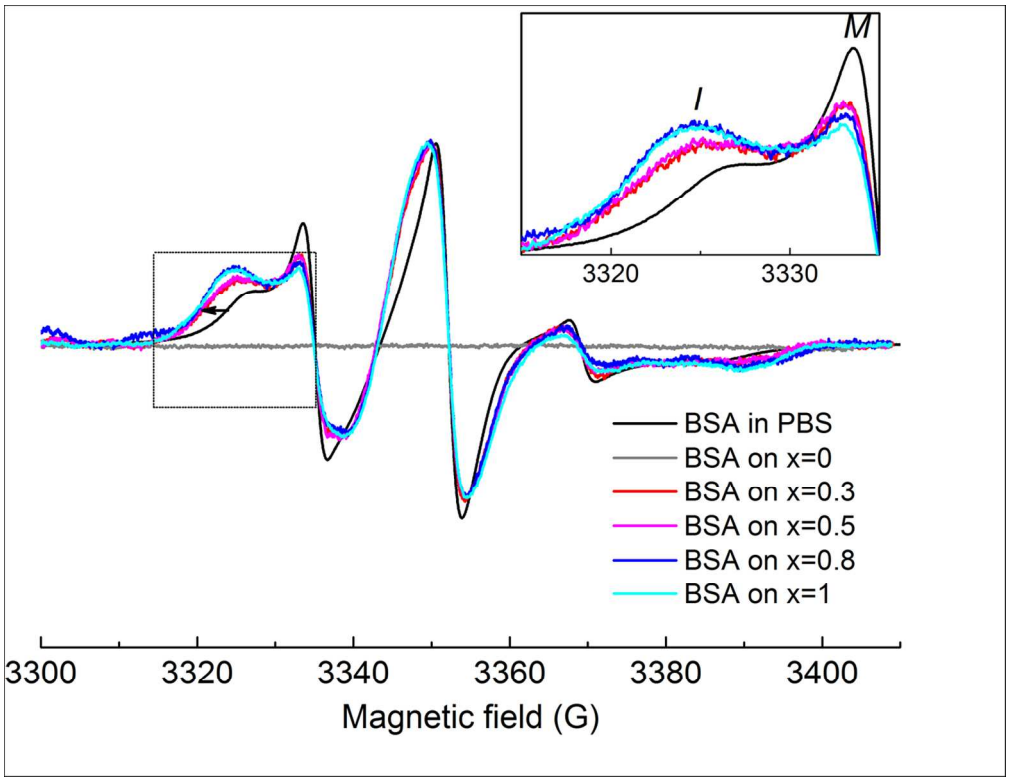

Figure 8
246x190mm (300 x 300 DPI)

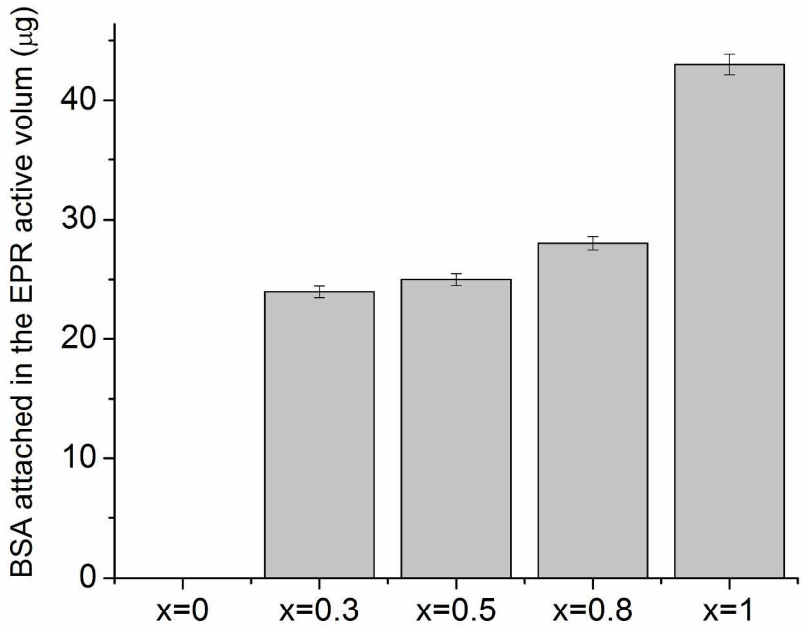

Fig. 9
279x215mm (300 x 300 DPI)

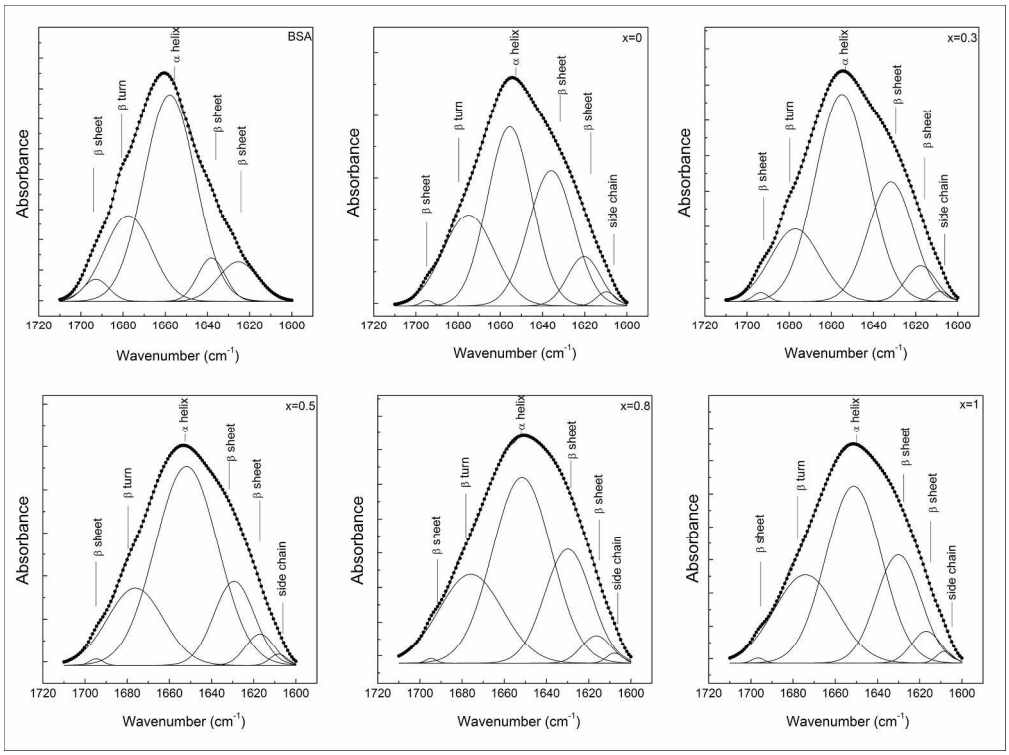

Fig. 10
474x353mm (300 x 300 DPI)

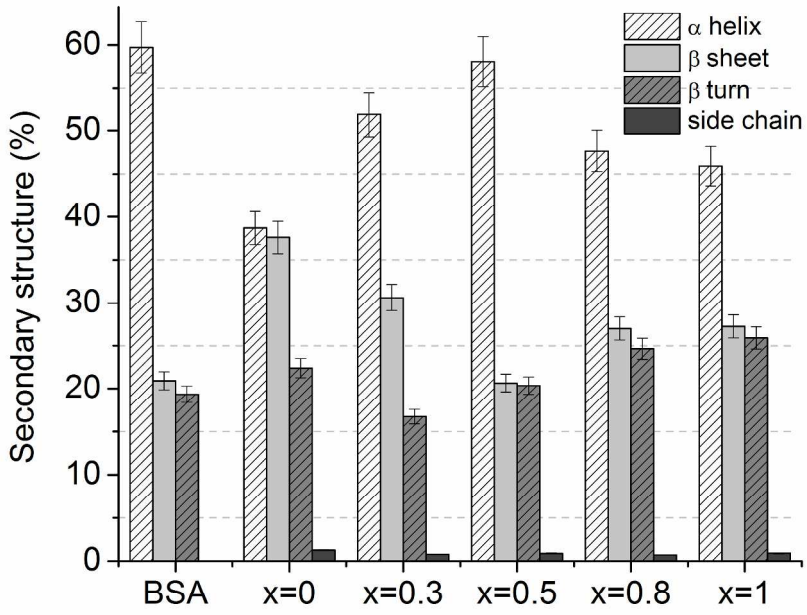

Fig. 11
279x215mm (300 x 300 DPI)

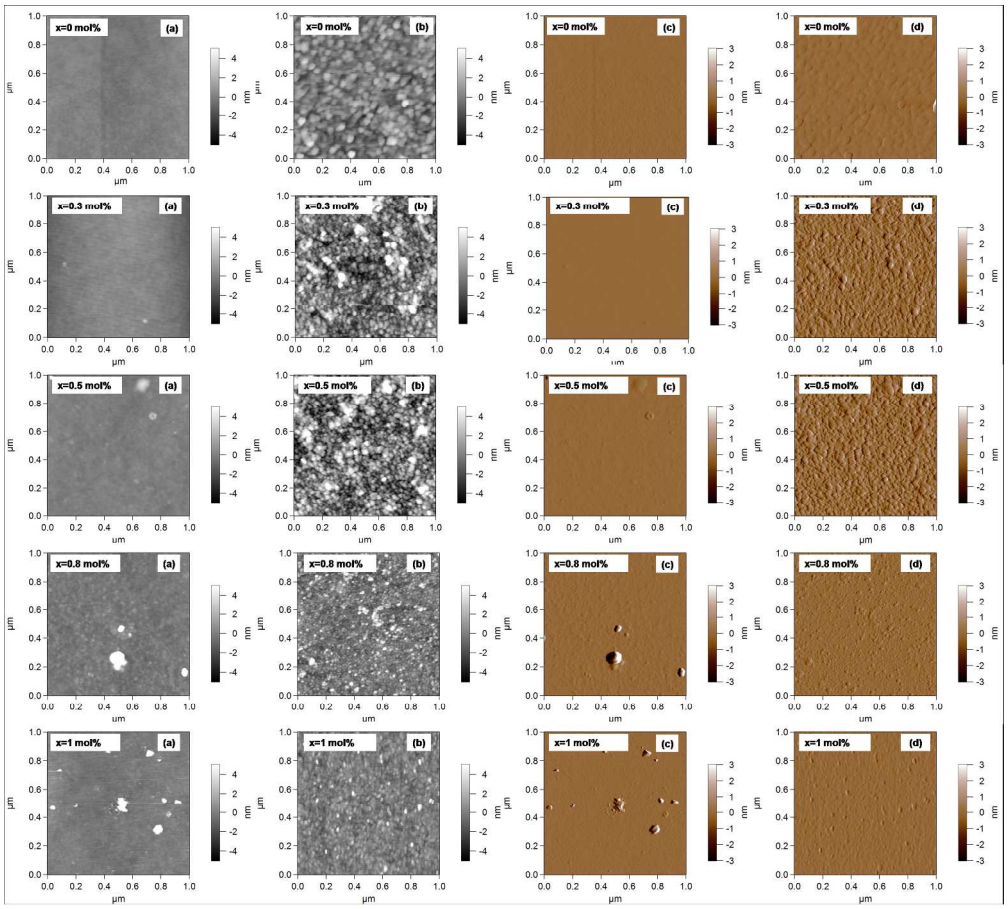

Figure 12
299x269mm (300 x 300 DPI)

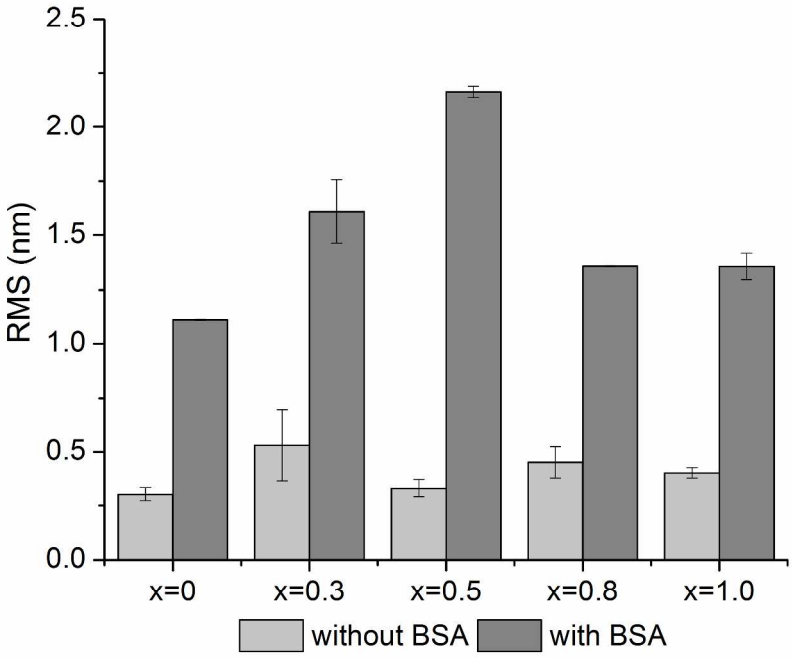

Figure 13
271x203mm (300 x 300 DPI)

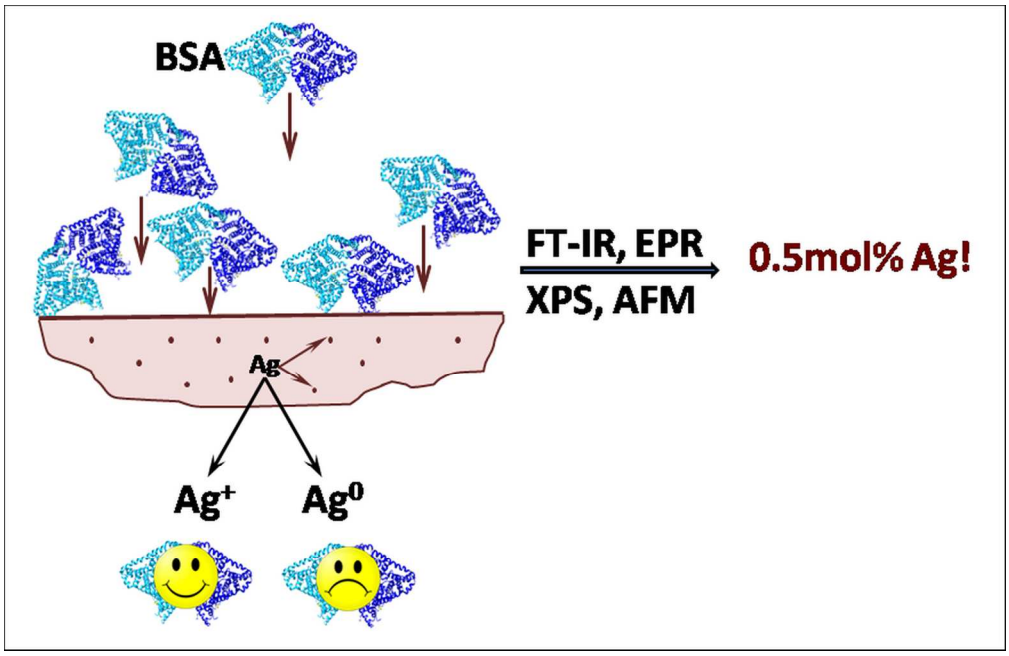

148x95mm (300 x 300 DPI)